

See discussions, stats, and author profiles for this publication at: <https://www.researchgate.net/publication/24040447>

Structural Basis for Inhibition of Mammalian Adenylyl Cyclase by Calcium

ARTICLE *in* BIOCHEMISTRY · MARCH 2009

Impact Factor: 3.02 · DOI: 10.1021/bi802122k · Source: PubMed

CITATIONS

33

READS

38

4 AUTHORS, INCLUDING:



Nanako Masada

17 PUBLICATIONS 414 CITATIONS

SEE PROFILE



Dermot Cooper

University of Cambridge

187 PUBLICATIONS 8,850 CITATIONS

SEE PROFILE

Published in final edited form as:

Biochemistry. 2009 April 21; 48(15): 3387–3397. doi:10.1021/bi802122k.

STRUCTURAL BASIS FOR INHIBITION OF MAMMALIAN ADENYLYL CYCLASE BY CALCIUM[†]

Tung—Chung Mou[‡], Nanako Masada[§], Dermot M. F. Cooper[‡], and Stephen R. Sprang^{‡,*}

[‡]Center for Biomolecular Structure and Dynamics and the Division of Biological Sciences, The University of Montana, Missoula, MT 59812

[§]Department of Pharmacology, University of Cambridge, Cambridge, CB2 1PD, United Kingdom.

Abstract

Type V and VI mammalian adenylyl cyclases (AC5, AC6) are inhibited by Ca²⁺ at both sub- and supra-micromolar concentration. This inhibition may provide feedback in situations where cAMP promotes opening of Ca²⁺ channels, allowing fine control of cardiac contraction and rhythmicity in cardiac tissue where AC5 and AC6 predominate. Ca²⁺ inhibits the soluble AC core composed of the C1 domain of AC5 (VC1) and the C2 domain of AC2 (IIC2). As observed for holo-AC5, inhibition is biphasic, showing “high affinity” ($K_i = \sim 0.4 \mu\text{M}$) and “low-affinity” ($K_i = \sim 100 \mu\text{M}$) modes of inhibition. At micromolar concentration, Ca²⁺ inhibition is non-exclusive with respect to pyrophosphate (PPi), a non-competitive inhibitor with respect to ATP, but at $> 100 \mu\text{M}$ Ca²⁺, inhibition appears to be exclusive with respect to PPi. The 3.0 Å-resolution structure of Gαs•GTPγS/forskolin-activated VC1:IIC2 crystals soaked in the presence of ATPαS and 8 μM free Ca²⁺ contains a single, loosely coordinated metal ion. ATP soaked into VC1:IIC2 crystals in the presence of 1.5 mM Ca²⁺ is not cyclized, and two calcium ions are observed in the 2.9 Å resolution structure of the complex. In both of the latter complexes VC1:IIC2 adopts the “open”, catalytically inactive conformation characteristic of the apoenzyme, in contrast to the “closed”, active conformation seen in the presence of ATP analogs and Mg²⁺ or Mn²⁺. Structures of the pyrophosphate (PPi) complex with 10 mM Mg²⁺ (2.8 Å) or 2 mM Ca²⁺ (2.7 Å) also adopt the open conformation, indicating that the closed to open transition occurs after cAMP release. In the latter complexes, Ca²⁺ and Mg²⁺ bind only to the high-affinity “B” metal site associated with substrate/product stabilization. Ca²⁺ thus stabilizes the inactive conformation in both ATP- and PPi-bound states.

The nine membrane-bound mammalian adenylyl cyclase (AC)¹ isoforms and a soluble AC (sAC) catalyze the conversion of ATP to the intracellular second-messenger cAMP and pyrophosphate (PPi) (1,2). Biochemical and crystallographic studies show that this enzymatic process requires Mg²⁺ or Mn²⁺ as co-factors (3-5). Membrane-bound ACs are activated by the stimulatory G protein α subunit (Gαs) and other regulatory molecules (1,6,7). The catalytic activity of several ACs is profoundly influenced by submicromolar Ca²⁺ (8,9). At resting physiological concentration of $\sim 100 \text{ nM}$ (10), calcium ions stimulate Type I and Type VIII isoforms of AC but inhibit Types V and VI. These isoforms, which are differentially expressed in tissues, integrate the effects of calcium- and cAMP-mediated signaling to control diverse cellular functions (11-13). Calmodulin mediates the calcium stimulation of both Type I and

[†]This work was supported by NIH Grant R01-DK46371 (S.R.S.) and Wellcome Trust grant RG31760 (DMFC). DMFC is a Royal Society Wolfson Research Fellow.

*Correspondence to: Stephen R. Sprang University of Montana Center for Biomolecular Structure and Dynamics 32 Campus Drive Missoula, MT 59812 phone: (406) 243 6028 Fax: (406) 243 4227 E-mail: Stephen.sprang@umontana.edu.

Type VIII AC and could contribute to mechanisms of learning and memory (14-17). Type III AC is regulated by calmodulin and CAM Kinase II (18,19), and Type IV is subject to calcium inhibition through the action of calcineurin (20). The two calcium-inhibited ACs (Type V and VI) are highly expressed in cardiovascular tissue and have been proposed to be key negative feedback regulators of cardiac rhythmicity (21-23). At high ($>10 \mu\text{M}$) concentration Ca^{2+} inhibits all mammalian AC isoforms (9,11,24,25).

The catalytic site of AC, as for all Class III cyclases, resides at the interface of two homologous Cyclase Homology Domains (CHD) (26). The model for the prototypical AC catalytic core is derived from crystal structures of the complex formed by the C1 CHD domain from AC5 and the C2 CHD domain from AC2 (VC1:IIC2) bound to two activators, forskolin (FSK) and GTP γ S-activated G α s (27). Structural studies of activated VC1:IIC2 complexes bound to substrate analogs show that the active site of AC contains two Mg^{2+} (or Mn^{2+}) sites, designated "A" and "B", that must be occupied for catalytic activity (5). Upon binding to potent substrate analogs, AC undergoes a transition from an "open" to a "closed" conformation by moving several structural elements in both CHDs toward the catalytic site. In the catalytically active conformation, both divalent metal ions coordinate with the substrate and with two conserved aspartic acid residues, Asp-396 and Asp-440 (residue numbers refer to AC5) in the C1 domain. The metal ion in site "A" is thought to activate the 3'-ribosyl hydroxyl group for nucleophilic attack on the oxygen of the α -phosphate whereas the metal ion in site "B" coordinates with β - and γ -phosphates of ATP (4,5). The ATP phosphates are themselves recognized by a phosphate binding loop at the junction of the C1 domain β 1- α 1 element. Kinetic analysis shows that cAMP is released from the enzyme more rapidly than the second product, pyrophosphate (PPi) (28). The enzyme adopts the open state upon product release, but it is not known whether the transition to this state occurs upon cAMP formation, or release of cAMP or PPi from the enzyme.

Previous studies have shown that Ca^{2+} inhibits AC5 and AC6, by a mechanism that is largely non-competitive with respect to ATP (9). Calcium ion antagonizes the activation of these enzymes by Mg^{2+} , and this inhibition is biphasic with respect to Ca^{2+} concentration (9,25, 29). Kinetic analysis of AC5 shows that, at submicromolar concentration, Ca^{2+} is a non-competitive inhibitor of Mg^{2+} activation, and, at supramicromolar concentration, Ca^{2+} inhibition is directly competitive with Mg^{2+} (25). The interdependence of Mg^{2+} activation and Ca^{2+} inhibition in site-directed mutants of AC5 suggests that inhibition of AC by Ca^{2+} involves the Mg^{2+} -binding loci at the AC catalytic site. Indeed, mutations distal to the Mg^{2+} coordination site that affected Mg^{2+} binding also displayed impaired or diminished Ca^{2+} -inhibition in direct proportion to diminution of activation by Mg^{2+} (25). That high-affinity Ca^{2+} binding is non-competitive with respect to Mg^{2+} is suggestive of an allosteric mode of action, wherein Ca^{2+} modulates the conformational equilibrium of the enzyme. However, the mechanisms by which Ca^{2+} regulates AC remain to be understood at the molecular level.

Here, we present structural data that provides insight into the molecular mechanism by which Ca^{2+} inhibits AC5. Ideally, such an investigation would focus on the AC5 holoenzyme, or its catalytic domain, which is subject to the same mechanism of Ca^{2+} inhibition (25). However, biochemical studies have demonstrated that the catalytic and many of the regulatory properties of holo-AC are faithfully recapitulated by the G α s-activated soluble VC1:IIC2 catalytic core of AC, which is amenable to crystallization (30,31). Experiments conducted with chimeric AC molecules demonstrate that isoform-specific high-affinity inhibition by Ca^{2+} is conferred by the C1 domain, but not the C2 domain of AC. Chimeric AC molecules composed of the Transmembrane 1 (TM1) and C1 domains of AC5 and the TM2 and C2 domains of AC2 retain susceptibility to inhibition submicromolar Ca^{2+} . In contrast, the corresponding constructs in which TM1/C1 is derived from AC2 and TM2/C2 from AC5, are not inhibited. High-affinity Ca^{2+} inhibition was also observed in experiments in which half molecules composed of the

TM and C1a (CHD only) domain of AC5 and the TM and C2 domain of AC2 were co-expressed (25). These experiments, together with evidence that Ca^{2+} acts at the Mg^{2+} cofactor binding sites, have prompted us to use $\text{Gas}\cdot\text{GTP}\gamma\text{S}:\text{VC1}:\text{IIC2}$ as a model system to investigate the structural mechanism for high-affinity inhibition of AC5 by Ca^{2+} .

Here, we present kinetic evidence to demonstrate that, in the presence of $\text{Gas}\cdot\text{GTP}\gamma\text{S}$ and FSK, Ca^{2+} shows the same pattern of high- and low-affinity inhibition towards $\text{VC1}:\text{IIC2}$ that has been observed for holo AC5. We have determined a series of crystal structures of $\text{Gas}\cdot\text{GTP}\gamma\text{S}$ and FSK-activated $\text{VC1}:\text{IIC2}$ in the presence of Ca^{2+} that provide direct insight into the mechanism of Ca^{2+} inhibition. These structures were determined, 1) in the presence of non-reactive ATP analog and free Ca^{2+} at a concentration below the EC_{50} for high affinity inhibition; 2) in the presence of ATP and free Ca^{2+} in the millimolar range sufficient to saturate both high and low affinity sites and 3) in the presence of pyrophosphate and saturating Ca^{2+} . In conjunction with the latter, we have also determined the structure of the $\text{Gas}\cdot\text{GTP}\gamma\text{S}$ and FSK-activated AC catalytic core bound to the cofactor Mg^{2+} and pyrophosphate, the binary product complex. Together, these structures elucidate the mode of Ca^{2+} binding in the high- and low-concentration regimes and show that Ca^{2+} stabilizes the inactive (open) state of the enzyme in both ATP and PPi -bound states. Further, the structure of the PPi -bound AC catalytic core provides insight into the nature of conformational changes that accompany the product-release phase of the AC catalytic cycle.

MATERIALS AND METHODS

Preparation of protein complexes

Recombinant mammalian adenylyl cyclase cytosolic VC1 and IIC2 domains and bovine Gas proteins were expressed and purified as described (32). Before complex formation, the Gas protein was activated by $\text{GTP}\gamma\text{S}$ and then trypsin-digested. A mixture of individually purified recombinant VC1, IIC2 and trypsin—treated $\text{Gas}\cdot\text{GTP}\gamma\text{S}$ was passed through sizing columns in the presence of excess MP-FSK and $\text{GTP}\gamma\text{S}$. Fractions containing the heterotrimeric complex were identified by gel electrophoresis on a 4-20% Tris-HCl polyacrylamide gel (BIO-RAD, Hercules, CA). Fractions containing the complex were collected and concentrated to ~8 mg/ml in a buffer containing 20 mM Na^+HEPES (pH 8.0), 2 mM EDTA, 2 mM MgCl_2 , 2 mM DTT, 100 mM NaCl, 25 μM MP-FSK, and 10 μM $\text{GTP}\gamma\text{S}$ for crystallization.

Crystallization, structure determination, and model refinement of the MP-FSK, $\text{Gas}\cdot\text{GTP}\gamma\text{S}:\text{VC1}:\text{IIC2}$ complex with substrates and Ca^{2+} or Mg^{2+}

Crystals of the protein complex were grown, harvested and cryoprotected as described previously (32,33). Before cryoprotection, crystals were soaked in one of following reservoir solutions: 2 mM $\text{ATP}\alpha\text{S}$ and 50 μM CaCl_2 (for which the free $[\text{Ca}^{2+}]$ was found to be 8 μM using the dye calibration method of Linse (34)); 5 mM ATP and 1.5 mM CaCl_2 ; 3 mM PPi and 10 mM MgCl_2 ; or 3 mM PPi and 2 mM CaCl_2 for 1-2 hr at room temperature and then harvested in cryoprotectant solution containing the same concentrations of the respective ligands and metal ions. For crystallization of mAC at low $[\text{Ca}^{2+}]$, crystals were soaked in reservoir solution containing 2mM $\text{ATP}\alpha\text{S}$ and 50 μM CaCl_2 , which were likewise present at the same concentrations in cryoprotectant solutions. Diffraction data sets were collected by the oscillation method at the Advanced Photon Synchrotron SBC-CAT ID-19 beamline or the Stanford Synchrotron Radiation Laboratory 9-1 beamline with an incident beam wavelength of 1.0454Å or 1.0231Å, respectively. Image processing and data reduction utilized the HKL2000 package (35). Due to anisotropy, data with I index > 20 for crystals of the $\text{Gas}\cdot\text{GTP}\gamma\text{S}$ and FSK-activated $\text{VC1}:\text{IIC2}$ complexes with $\text{PPi}\cdot\text{Mg}^{2+}$, $\text{PPi}\cdot\text{Ca}^{2+}$, $\text{ATP}\alpha\text{S}\cdot\text{Ca}^{2+}$, or $\text{ATP}\cdot 2\text{Ca}^{2+}$ were excluded from the dataset used for refinement. The atomic coordinates from the isomorphous crystals of the MP-FSK, $\text{Gas}\cdot\text{GTP}\gamma\text{S}:\text{VC1}:\text{IIC2}$ complex

(PDB code: 1AZS), were used to compute initial phases for all four complexes (27). Atomic positions and thermal parameters were refined by successive rounds of rigid body refinement, simulated annealing, Powell minimization, and B factor refinement using the CNS 1.1 program suite (36) or REFMAC5 (37) as implemented in the CCP4 program Suite (38). Ligands and metal ion(s) were located in SIGMA—A weighted (39) difference omit maps computed with phases from refined models. Atomic models were iteratively improved by manual refitting into weighted $2|Fo|-|Fc|$ maps using the computer graphics model building programs O and Coot (40,41), and subsequent cycles of refinement using CNS or REFMAC5. Diffraction and refinement statistics are given in Table 1. Figures were generated using PyMOL (DeLano Scientific LLC, San Carlos, CA. <http://www.pymol.org>). Coordinates for the AC•PPi•Ca²⁺, AC•PPi•Mg²⁺, AC•ATP•2Ca²⁺ and AC•ATPαS•Ca²⁺ complexes have been deposited in the Protein Data Bank with the codes 3C14, 3C15, 3C16, and 3E8A, respectively.

Measurement of adenylyl cyclase activity

Adenylyl cyclase activity was determined as described previously (42-44) with some modifications. Briefly, for measurement of Ca²⁺ inhibition of Mg²⁺, FSK, Gas•GTPγS activated VC1:IIC2, adenylyl cyclase activity of purified VC1 (50 nM) and IIC2 (250 nM) was measured in the presence of the following components: 12 mM phosphocreatine, 2.5 units of creatine phosphokinase, 0.1 mM cAMP, 0.1 mM ATP, 0.04 mM GTP, 0.5 mM phosphodiesterase inhibitor, isobutylmethylxanthine, 1.25 μCi of [α -³²P]ATP, 0.75 mM MgCl₂, 10 μM FSK or 500nM Gas•GTPγS, as indicated. Free Ca²⁺ concentrations were established using an EGTA-buffering system as described previously (45) and the BAD4 computer program (24). The reaction mixture (final volume, 100 μl) was incubated at 30 °C for 20 min. Reactions were terminated with sodium lauryl sulfate (0.5%); [8-³H]cAMP (~6000 cpm) was added as a recovery marker, and the [³²P]cAMP formed was quantitated as described previously (46).

For PPi or Ca²⁺/PPi inhibition experiments, the activity of purified VC1 (100 nM) and IIC2 (500 nM) was measured in a buffer of 25mM Na⁺Hepes (pH 8.0) containing 20mM phosphor (enol)pyruvate, 0.1 mM GTP, 3 units pyruvate kinase, 0.1mM ATP, 0.1mM cAMP, 0.3 mM MgCl₂, 1 μCi of [α -³²P]ATP, 1 μM Gas•GTPγS, and 100 μM FSK, unless stated otherwise. Free Ca²⁺ concentrations were established and calibrated using an EGTA-buffering system as described previously (34). Following a 2 min pre-incubation at 37°C, reactions were conducted for 15 min at 37°C and were terminated by the addition of 20 μL of 2.2 N HCl containing [³H]cAMP. Denatured protein was additionally heated to 95°C for 4 min, cooled on ice, and finally sedimented by a 1 min centrifugation at 15,000 × g. Reaction mixtures were applied onto disposable columns filled with 1.3 g neutral alumina. cAMP was separated from [α -³²P]ATP by elution of cAMP with 0.1 M ammonium acetate, pH 7.0. [³²P]cAMP and [³H]cAMP was measured by liquid scintillation spectrometry where [³H]cAMP was calculated for the efficiency of cAMP recovery of each tube. Nonlinear regression curves and kinetic parameters were obtained using SigmaPlot software (SYSTAT Software Inc, San Jose, CA). Adenylyl cyclase activity is expressed per weight of VC1 and data points are presented as mean activities ± S.D. of triplicate determinations.

Measurement of ATP synthesis

The measurement of ATP synthesis from cAMP and PPi was performed as described previously (28) with some modifications. The reverse reaction of adenylyl cyclase was measured spectrophotometrically in the presence of the following components: 50 mM glucose, 20 mM Hepes, 1.2 units of hexokinase, 0.8 mM NADP, 2 mM MgCl₂, 2 mM PPi, 0.5 units of glucose-6-phosphate dehydrogenase, and the various concentrations of cAMP and CaCl₂. The reaction was started by the addition of 0.4 μM VC1, 2 μM IIC2, and 1 μM Gas•GTPγS (final volume 400 μl, pH 7.4), incubated at 30 °C for 40 min. ATP synthesized was determined by the rate of NADP reduction as measured by the change in absorbance at

340 nm using an a Ultrospec 2100 Pro UV/Visible spectrophotometer. A standard curve was obtained by measuring the rate of NADP reduction at a range of ATP concentration in the absence of protein, cAMP, and PPI. ATP synthesis activities were expressed per weight of VC1 and fitted with Lineweaver-Burk analysis using GraphPad Prism Version 4. Data points were presented as mean activities \pm S.D. of triplicate determinations.

Chemicals

GTP γ S was obtained from Roche (Indianapolis, IN). FSK and MP-FSK were obtained from Merck (Nottingham, UK) or Calbiochem (La Jolla, CA). [α - 32 P]ATP (3,000 Ci/mmol) was from Perkin—Elmer Life Sciences (Boston, MA) or GE Healthcare (Little Chalfont, UK). [8- 3 H]cAMP were obtained from GE Healthcare (Little Chalfont, UK) and all other reagents were purchased from Sigma (Poole, UK).

RESULTS

Ca $^{2+}$ inhibition of activated VC1:IIC2

As noted in the introduction, Ca $^{2+}$ was shown to exert biphasic inhibition of AC5 and AC6 in cell lysates (9,25). In the present work, we extended these studies to investigate Ca $^{2+}$ inhibition of a purified soluble recombinant complex consisting of VC1 and IIC2. This complex possesses high catalytic activity upon activation by both FSK and Gs α •GTP γ S protein (31), and thus experiments were conducted in the presence of 10 μ M FSK and 500 nM Gs α •GTP γ S. As is the case for holoenzyme preparations, inhibition of FSK and Gs α •GTP γ S activated VC1:IIC2 by Ca $^{2+}$ is biphasic (Figure 1A), with EC $_{50}$ values of 0.37 ± 0.03 μ M and 100 ± 30 μ M, respectively. The K_i of the high affinity component is not significantly changed, whereas that of the low affinity inhibition increased two-fold over the range of [Mg $^{2+}$] from 0.3 mM to 3 mM (data not shown). These results are comparable to data taken from cell lysates expressing AC5 where the range for high and low affinity of Ca $^{2+}$ inhibition was 0.28 ± 0.21 μ M and $32 - 163$ μ M, respectively (25) indicative of non-competitive and competitive inhibition of Mg $^{2+}$ activation of AC through the high- and low-affinity binding modes of Ca $^{2+}$.

Inhibition of VC1:IIC2 by PPI and Ca $^{2+}$

AC activity in the direction of cAMP synthesis is inhibited by both reaction products, cAMP and PPI (28). Product inhibition by PPI has been shown to be non-competitive with respect to ATP with an observed K_i of ~ 300 μ M. Over a range of PPI concentrations, Ca $^{2+}$ exhibits biphasic inhibition of VC1:IIC2 in the presence of Gs α •GTP γ S and FSK (Figure 1A). A Dixon plot of 1/velocity *versus* the concentration of Ca $^{2+}$ in the high affinity range (200 nM – 1.4 μ M) intersect at a common point, consistent with non-exclusive inhibition by Ca $^{2+}$ and PPI of adenylyl cyclase (47) (Figure 1B, upper panel). The K_i of PPI remains constant over this range of Ca $^{2+}$, indicating that the two inhibitors do not bind cooperatively. Values of reciprocal velocity at varying [PPI] at [Ca $^{2+}$] in the low affinity range (30 – 300 μ M) give rise to a set of parallel lines, indicating that PPI and Ca $^{2+}$, acting at a low-affinity site, are exclusive inhibitors (Figure 1B, lower panel). These kinetic data can be rationalized by the crystal structures of Ca $^{2+}$ complexes with VC1:IIC2 described below. The origin of the sharp rise in AC activity in the 2.5 - 5 μ M Ca $^{2+}$ range, observed in the presence of PPI is not apparent. It is possible that, in this narrow concentration range, Ca $^{2+}$ potentiation of ATP binding offsets the combined inhibitory affects of Ca $^{2+}$ and PPI on catalytic activity.

Effect of Ca $^{2+}$ inhibition on ATP synthesis

To determine whether Ca $^{2+}$ is an inhibitor of AC in the direction of ATP synthesis, we measured the rate of ATP production from cAMP and PPI in the presence of Mg $^{2+}$ at various Ca $^{2+}$ concentrations. The reverse reaction, like the forward reaction, is also activated by Gs α •GTP

and FSK, but with less potency (28). Double reciprocal plot analysis shows that Ca^{2+} causes a slight increase in the K_m for cAMP, and no significant change in V_{\max} . However, the inhibitory potency of Ca^{2+} reaches a plateau in the 2 μM to 5 μM range. Thus, Ca^{2+} appears to be a competitive partial inhibitor with respect to cAMP in the direction of ATP synthesis (Figure 2) with an inhibition constant similar to that for “high affinity” inhibition of cAMP synthesis.

Crystal structure of the VC1:IIC2 complex with Ca^{2+} and ATP αS or ATP

We determined the structure of the $\text{Gas}\cdot\text{GTP}\gamma\text{S}/\text{FSK}$ -bound VC1:IIC2•ATP αS -R_p complex from crystals soaked in reservoir solution containing 8 μM free Ca^{2+} , well below the K_i for low-affinity Ca^{2+} inhibition. The isosteric and non-reactive ATP analog ATP αS -R_p was used in this instance because VC1:IIC2 retains appreciable catalytic activity in the presence of micromolar Ca^{2+} . The structure of the VC1:IIC2•ATP complex was also determined from crystals containing 1.5 mM Ca^{2+} , sufficient to achieve maximal inhibition. The structures of the two complexes were determined at 3.0 Å (ATP αS -R_p) and 2.9 Å (ATP) resolution (Table 1), and are isomorphous with previously reported $\text{Gas}\cdot\text{GTP}\gamma\text{S}/\text{FSK}$ -bound VC1:IIC2 structures (27). Both the Ca^{2+} -bound ATP and ATP αS -R_p complexes adopt the “open” conformation characteristic of apo-VC1:IIC2 (Figure 3A), in contrast to the “closed” state seen in the complex of ATP αS -R_p with Mg^{2+} and Mn^{2+} (5). In the open state, the enzyme is not able to form the full complement of protein-nucleotide interactions that are possible for the closed state. Although VC1:IIC2 adopts an open conformation in both complexes, the mode of nucleotide- Ca^{2+} binding in the “low- Ca^{2+} ”, ATP αS -R_p complex differs significantly from that in the “high- Ca^{2+} ” complex with ATP. The enzyme active site of the latter adopts a more open conformation due to a rotation of the C1 domain $\alpha 1$ helix away from the subunit interface (Figure 3B).

The ($|F_o| - |F_c|$) difference electron density map, for the ATP αS -R_p complex reveals continuous density for ATP αS -R_p and a single diffuse peak which we attribute to a Ca^{2+} ion (Figure 4A). This assignment is confirmed by the presence of positive difference density observed upon modeling a water molecule at that site (Figure 4B). Magnesium ion, which could be expected to bind in similar fashion, was not present in the soaking solution. We refer to this structure as the ATP $\alpha\text{S}\cdot\text{Ca}^{2+}$ complex.

The nucleotide in the ATP $\alpha\text{S}\cdot\text{Ca}^{2+}$ complex adopts a compact, arched conformation. The electron density, together with stereochemical constraints imposed during refinement dictate a *gauche* conformation for the C(4')-C(5') ribosyl bond, and a glycosyl bond angle in the mid-*anti* range, which together cause the α thiophosphate to project away from the metal center. This mode of ATP αS -R_p binding contrasts with that in the “closed:” complex with Mg^{2+} and Mn^{2+} bound to the metal A and B sites, respectively (5) (Figure 5A,B). The purine ring of ATP αS -R_p in the Ca^{2+} complex is within hydrogen bonding distance of the carbonyl oxygen atom of Ile-1019, affording interactions that provide specificity for adenine in preference to other nucleotide bases (26,48,49). However, as a consequence of the compact configuration of the nucleotide, and the open conformation of VC1:IIC2, the β and γ phosphate moieties cannot form hydrogen bonds with main-chain amides in the $\beta 1$ - $\alpha 1$ loop of VC1 (Figure 5B). The diffuse electron density for these phosphate moieties is indicative of a flexible binding mode.

The single Ca^{2+} ion observed in the ATP $\alpha\text{S}\cdot\text{Ca}^{2+}$ complex occupies a position intermediate between the Mg^{2+} A and B sites (Figure 5B), although it is coordinated by the β and γ phosphates and both Asp-396 and Asp-440 as is typical for B-site metal interactions (5). As noted above, the α thiophosphate is not within coordination distance of the calcium ion. Electron density extending from the ribosyl group to the Ca^{2+} can be modeled as a water molecule bridging the ribose O(3') and the calcium ion (Figure 4A). Even at the modest

resolution of the structure, it is apparent that Ca^{2+} - oxygen ligand distances are longer than typically observed in protein- Ca^{2+} complexes, indicating that the metal is not rigidly coordinated (50).

The crystal structure of $\text{G}\alpha\text{s}\cdot\text{GTP}\gamma\text{S}/\text{FSK}$ -activated VC1:IC2 bound to ATP in the presence of millimolar Ca^{2+} exhibits two Ca^{2+} ions at the metal-binding site (Figure 4C). An $|F_o| - |F_c|$ electron density map computed with refined coordinates of the protein and bound nucleotide, show difference density at both Ca^{2+} sites, as well as weaker density that we attribute to ordered water molecules (Figure 4D). Accordingly, we refer to this structure as the $\text{ATP}\cdot 2\text{Ca}^{2+}$ complex. The metal ions are separated by only 3 Å, well under the separation distance expected for adjacent calcium ions. It is possible that the observed distance is an artifact of static disorder, as discussed below. The nucleotide triphosphate exhibits an extended conformation similar to that of $\text{ATP}\alpha\text{S}\text{-R}_p$ in the closed complex with Mg^{2+} and Mn^{2+} , but is translated about 1 Å towards the $\beta 1$ - $\alpha 1$ relative to the latter (Figure 6A,C). This relative translation may be due to the expansion of the metal coordination sphere required to accommodate two calcium ions, which have larger radii (1.14 Å) than Mg^{2+} (0.86 Å) and Mn^{2+} (0.89 Å). The expansion of the coordination sphere forces the metal ligands in the $\beta 1$ - $\alpha 1$ loop (carboxylate of Asp 396 and carbonyl oxygen of Ile 397) away from the catalytic site, with the collateral loss of interactions between the ATP β and γ phosphates and the main chain amides of Gly-399 and Phe-400 observed in the closed conformation of VC1:IC2. Consequently, the CHD domains of $\text{ATP}\cdot 2\text{Ca}^{2+}$ adopt a somewhat more open conformation than that of $\text{ATP}\alpha\text{S}\cdot\text{Ca}^{2+}$, such that $\alpha 1$ helix is rotated about 10° further away from the C1:C2 interface (Figure 3B). Likewise, the adenosine moiety is not close enough to Asp-1018 and Ile-1019 to form hydrogen bonds or van der Waals contacts with these side chains in the base recognition pocket (Figure 6A,C). Further, the more open conformation at the C1:C2 domain interface does not allow for an ion pair interaction between Arg-1029 of the C2 domain with the α -phosphate oxygen atoms of ATP as observed in the $\text{ATP}\alpha\text{S}\cdot\text{Mn}^{2+}\cdot\text{Mg}^{2+}$ complex. This interaction has a key role in transition state stabilization (27, 51, 52).

Water-mediated interactions contribute to ATP binding in the open complex with Ca^{2+} . In the closed state, Lys-1065 of the C2 domain $\beta 7'$ - $\beta 8'$ hairpin loop forms ionic contacts with α - and γ -phosphates of the nucleotide. In the $\text{ATP}\cdot 2\text{Ca}^{2+}$ complex, this ionic interaction is mediated by a water molecule (Figure 4C,D and 5C). A network of water molecules tethers ATP to Ca^{2+} and protein. The 3'-hydroxyl of the ribose forms water-mediated contacts with the A site Ca^{2+} . The triphosphate of ATP is also stabilized by a water molecule that coordinates with two oxygen atoms of the β - and γ -phosphates and two backbone amine groups of Gly-399 and Phe-400 (Figure 4D, 5C) at the N-terminus of the C1 domain $\alpha 1$ helix. These hydrogen bonds match those interactions between the $\beta 1$ - $\alpha 1$ loop and triphosphates of $\text{ATP}\alpha\text{S}$ in the closed state. Thus, $\text{ATP}\cdot 2\text{Ca}^{2+}$ is accommodated in the catalytic site despite the loss of direct interactions with C2 domain while retaining contacts with the C1 domain. These observations are consistent with the evidence that the C1 domain mediates the effect of Ca^{2+} on the catalytic activity of AC (25).

The triphosphate moiety of ATP is fully engaged in coordination of the two Ca^{2+} ions in the $\text{ATP}\cdot 2\text{Ca}$ complex. The resolution of the structure does not permit accurate determination of Ca^{2+} -ligand coordination distances, yet the probable protein ligands can be identified. The equatorial plane of Ca^{2+} ligands comprises an α phosphate oxygen, one or both carboxylate oxygen atoms of Asp-396 and a water molecule. On one face of the equatorial plane, an axial ligand is provided by a carboxylate oxygen of Asp-440, while the opposite face is empty, possibly occupied by a disordered water molecule. The A-site Ca^{2+} is shifted about 2 Å closer to the Asp-396 carboxylate than the corresponding Mg^{2+} of the closed $\text{ATP}\alpha\text{S}$ complex, and so is able to form more contacts with protein ligands than the latter. The B-site Ca^{2+} is still more tightly bound with nearly hexadentate geometry. The equatorial plan is populated by one

oxygen atom of Asp-440, a β phosphate oxygen, the backbone carbonyl oxygen of Ile-397, and the ATP α - β phosphate bridging oxygen. A carboxylate oxygen of Asp-396 and the ATP γ phosphate contribute axial oxygen ligands. This mode of Ca^{2+} coordination is nearly identical to that observed for Mn^{2+} in the closed complex with ATP α S.

Structures of VC1:IIC2 bound to pyrophosphate and Ca^{2+} or Mg^{2+}

Crystals of VC1:IIC2 bound to PPI in conjunction with either Ca^{2+} or Mg^{2+} diffracted to 2.7Å and 2.8Å resolution, respectively (Figure 6). These represent, to our knowledge, the first structures to be determined of a AC terminal product complex with pyrophosphate. Comparison with the unliganded enzyme shows that the $\beta 1$ — $\alpha 1$ — $\alpha 2$ and $\alpha 3$ — $\beta 4$ loops of VC1 and $\beta 7'$ — $\beta 8'$ of IIC2 in the $\text{PPI}\cdot\text{Ca}^{2+}$ - and $\text{PPI}\cdot\text{Mg}^{2+}$ -bound complexes conform to the open conformation of AC (Figure 3A). Global and local structural differences among apo VC1:IIC2 and the $\text{PPI}\cdot\text{Ca}^{2+}$, and $\text{PPI}\cdot\text{Mg}^{2+}$ complexes are minimal with root mean square deviations among equivalent Ca positions of 0.41 – 0.55 Å.

The electron density omit map for both the $\text{PPI}\cdot\text{Mg}^{2+}$ and $\text{PPI}\cdot\text{Ca}^{2+}$ complexes of VC1:IIC2 can be unambiguously fit to a model consisting of pyrophosphate bound to a magnesium ion with a water molecule, or a single calcium cation, respectively (Figure 6A and 6B). Superposition of $\text{PPI}\cdot\text{Ca}^{2+}$ -bound VC1:IIC2 complex with that of the enzyme bound to $\text{Mg}^{2+}/\text{Mn}^{2+}$ and ATP α S, confirms that the calcium ion binds to the metal B site in the pyrophosphate complex. Difference Fourier analysis of the diffraction data obtained from crystals soaked in $\text{PPI}\cdot\text{Ca}^{2+}$ and $\text{PPI}\cdot\text{Mg}^{2+}$ revealed strong $|F_{\text{Ca}}^{\text{obs}} - F_{\text{Mg}}^{\text{obs}}|$ difference electron density at the metal “B” site (Figure 6D) confirming that the B site contains Ca^{2+} in the former complex. Neither the PPI complex with Mg^{2+} nor that with Ca^{2+} show electron density at the metal A site.

The orientation of pyrophosphate in the active site of the open state AC complexes described here differs from the β - γ diphosphate moiety of ATP α S in the closed state complex with Mg^{2+} and Mn^{2+} (5) (Figure 4B) and from pyrophosphate in the closed complex with the P-site analog 2'-d-3'-AMP (53). Essentially, the $\text{P}\beta$ - $\text{P}\gamma$ axis of the pyrophosphate rotates in conjunction with the change in the orientation of the C1 domain $\alpha 1$ helix in the transition from the closed to the open states of the enzyme. Consequently, hydrogen bond contact between the backbone amide groups of the $\alpha 1$ helix and PPI is maintained in both open and closed conformations. In the open state complexes with Mg^{2+} or Ca^{2+} , the PPI phosphate distal to the C1 domain $\alpha 1$ helix ($\text{P}\gamma$) is located in approximately the same position as the γ phosphate of the substrate analog in the ATP α S complex (Figure 4B) and its counterpart in the 2'-d-3'-AMP•PPI complex (5) (Figure 7). An oxygen atom from $\text{P}\gamma$ forms ion pair bonds with the positively charged guanidinium amides of Arg-484 from VC1 as seen in other structures of AC bound to substrate analogs, “P-site” and fluorophore-substituted inhibitors (Figure 6C) (5,33,53,54). The proximal phosphate ($\text{P}\beta$) is oriented toward the $\beta 1$ — $\alpha 1$ loop of VC1 and forms hydrogen bonds with the backbone amides of Gly-399 and Phe-400. This is in contrast to the closed complex with 2'-d-3'-AMP•PPI, where the PPI $\text{P}\gamma$ phosphate forms hydrogen bonds with the amide of Gly-399, and the proximal phosphate is hydrogen bonded to the amide groups of Phe-400 and Thr-401 (53). Thus, the $\text{P}\beta$ - $\text{P}\gamma$ axis of the pyrophosphate, which is aligned with the peptide bonds of residues 399-401 in the closed P-site complex, rotates $\sim 35^\circ$ in the $\text{PPI}\cdot\text{Ca}^{2+}(\text{Mg}^{2+})$ complexes. This rotation allows the $\text{P}\gamma$ moiety to maintain hydrogen bond contact with the $\alpha 1$ helix as it swings into the open state (Figure 7).

The amino acid side chains that interact with the metal ion and PPI maintain similar conformations in the Ca^{2+} and Mg^{2+} complexes with two significant exceptions. First, Asp-396 adopts a different rotameric state in the complex with Ca^{2+} , wherein both carboxylate oxygen atoms contact the metal ion, in comparison to the Mg^{2+} complex, in which only one of the carboxylate oxygen atoms is a metal ligand (Figure 6C-D). Secondly, Lys-1065 forms an ion

pair with the bridging oxygen of PPi in the PPi•Mg²⁺ complex but not in the complex with Ca²⁺. It appears that the loss of this ionic interaction is compensated by an additional coordinating contact between the P β phosphate and the metal ion. Interactions between Lys-1065 and phosphate groups of substrate analogs are generally observed in complexes with ATP analogs or fluorophore-substituted nucleotides, in which the enzyme adopts a closed or semi-closed conformation (5, 54)

B site Ca²⁺ coordination in the PPi complex is heptadentate, with some differences in the atoms that form the coordination sphere. A carboxylate oxygen of Asp-396 and an oxygen atom of P γ form axial ligands, and five equatorial ligands contributed by Asp-396, Asp-440, the carbonyl of Ile-397 and P β form a rough pentagonal array. B-site Mg²⁺ coordination in the PPi•Mg²⁺ complex is, in contrast, octahedral, involving oxygen ligands from P β , three VC1 residues (Asp-396, Asp-440, and Ile-397), and a water molecule (Figure 6C) but no interaction with P γ . The mode of PPi — metal coordination observed here differs from that in the closed complex with 2'-d-3'-AMP•PPi•Mg²⁺ a mimic of the cAMP•PPi complex, where the 3' nucleotide phosphate serves as the axial ligand of the B-site metal in place of a water molecule (53). In the closed complex with ATP α S, the α -thiophosphate acts in a similar role (Figure 5A). In both of the latter complexes the P γ of PPi, or the corresponding nucleotide γ phosphate, participates in metal coordination.

DISCUSSION

The data presented here provide strong evidence that Ca²⁺ inhibits AC5 by displacing the Mg²⁺ co-factors at the catalytic site. Accordingly, mutations of residues adjacent to (Cys-441 or Tyr-442) or remote from (Phe-423 and Arg-434) the Mg²⁺ binding site that diminish sensitivity of AC5 to inhibition by Ca²⁺ also impair enzyme activation by Mg²⁺ (25). Further, Ca²⁺ stabilizes an open, catalytically inactive conformation of the C1 and C2 domains of AC. This is the case for both the substrate complex with ATP and pyrophosphate product complex. Because AC assumes an open conformation in the PPi-bound state, Ca²⁺ inhibits AC by stabilizing the enzyme:product complex.

The biphasic inhibition of AC5 by Ca²⁺ is recapitulated in the hybrid catalytic core composed of VC1 and IIC2. Inhibition by Ca²⁺ at micromolar concentration, a hallmark of AC5 and AC6, arises from binding at a location close to the A site. However, coordination of the metal is B site-like, such that Ca²⁺ is loosely bound in an electronegative cage formed by the β and γ phosphates of ATP and by Asp-396 and 440. In this complex the substrate analog ATP α S adopts an arched conformation that does not permit interaction of its α phosphate with either Ca²⁺ or with residues, such as Arg-1029 that provide transition state stabilization (Figure 5B) (27). The compact conformation of the nucleotide is unlikely to be due to the presence of the Rp thiolate at the α phosphate since ATP α S adopts an extended conformation in the closed-state complex with Mg²⁺ and Mn²⁺ (Figure 5A) (5).

The non-competitive relationship reported earlier between Mg²⁺ activation and high-affinity Ca²⁺ inhibition (9) arises in part from stabilization, by Ca²⁺, of an open conformation of the ATP α S•Ca complex. Further, because the nucleotide β and γ phosphates are engaged in binding Ca²⁺ near the A site, they are unavailable for Mg²⁺ binding at site B. A conformational transition, similar to that which occurs upon binding a second calcium ion (see below), could accommodate Mg²⁺ at the B site, leaving Ca²⁺ bound to site A. However, unlike Mg²⁺, a calcium ion would not activate the O-3' hydroxyl of ATP for nucleophilic attack upon the α phosphate. Thus, A-site Ca²⁺ binding is inhibitory.

At ~100 μ M concentration, Ca²⁺ binds to both A and B sites of open-state VC1:IIC2. Because, at that concentration a calcium ion is already bound to AC with B site-like coordination, it is

likely that A site coordination is responsible for the low-affinity limb of the biphasic Ca^{2+} inhibition pattern. Binding of the second Ca^{2+} could be accompanied by translation of the first-bound Ca^{2+} to the B-site locus. This is likely to occur in concert with the conformational transition of ATP to an extended conformation (Figure 6C) (supplementary movie). However, because the expanded Ca^{2+} coordination sphere does not permit direct interactions between the β and γ ATP phosphate with the $\beta 1$ - $\alpha 1$ loop, AC remains in the open conformation. Rather, these phosphate moieties form water-mediated interactions with the amide groups in the open form of that loop. Bound to the open conformation of AC, ATP is miss-aligned with the catalytic residues. Interaction of Arg-1029 with the α phosphate of ATP, which provides transition-state stabilization, and hydrogen bonding of Asn-1025 to the ribose endocyclic oxygen, which may be important for substrate orientation (5), do not occur in the Ca^{2+} Complex (Figure 4D). Non-productive binding, and the failure of Ca^{2+} to provide catalytic activation at the A site, ensures that ATP does not turn over in crystals of Ca^{2+} -bound VC1:IIC2.

The distance between the two Ca^{2+} ions bound to the A and B sites of the $\text{ATP}\cdot 2\text{Ca}$ complex is considerably less than that observed between adjacent divalent ions (Mg^{2+} or Mn^{2+}) that share coordinating ligands in other mAC complexes (5) or in RNA polymerase (55). The ionic radius of Ca^{2+} is larger than that of Mg^{2+} and Mn^{2+} , consistent with separations between adjacent calcium ions ranging from 3.8 - 4.3 Å in the 2.5 Å resolution structure of the C2 domain of protein kinase C β (56). It is possible that the more weakly bound site A Ca^{2+} is partially occupied, such that the B site Ca^{2+} comes to occupy an intermediate position in asymmetric units in which Site A is unfilled. The Ca^{2+} positions reported here only represent average values for the two calcium ions in the refined structures. In fact, the distances between the two calcium ions range from 2.8 to 4.5 Å depending on the refinement constraints, consistent with dynamic interactions among two calcium ions, ATP, and neighboring protein residues and the modest resolution to which the crystals of the $\text{ATP}\cdot 2\text{Ca}$ complex diffract.

Product release from AC does not follow an obligate ordered mechanism, but cAMP dissociates more rapidly than pyrophosphate from the catalytic site (28). The structural data reported here are consistent with the hypothesis that AC reverts to an open conformation upon release of cAMP, while pyrophosphate and Mg^{2+} are still bound to the enzyme. Mg^{2+} occupies the B site at this stage of the catalytic cycle, and is tethered in an octahedral coordination sphere to oxygen atoms of the $\text{P}\beta$ pyrophosphate phosphate, and to the two conserved, and catalytically essential aspartate residues at positions 396 and 440. Hence, in the absence of stabilizing interactions with the purine moiety of the adenine nucleotide, and of metal-ion mediated interactions that link the nucleotide monophosphate and pyrophosphate groups, AC reverts to the relaxed, open conformation. The structure of the $\text{PPi}\cdot\text{Mg}^{2+}$ complex shows that PPi is a non-competitive inhibitor of AC because it stabilizes an open conformation of the enzyme to which ATP cannot bind productively.

High-affinity Ca^{2+} inhibition is non-exclusive with respect to pyrophosphate (Figure 1B), but appears to be exclusive at the low-affinity site. Even at millimolar concentration, only a single Ca^{2+} is bound to the $\text{VC1:IIC2}\cdot\text{PPi}$ complex, where it occupies the Mg^{2+} B site, and forms similar interactions with PPi and the conserved aspartate residues. The exclusivity between inhibition by PPi and by Ca^{2+} acting at the low-affinity site is probably due to the absence of the low-affinity A site in the open complex to which PPi binds. The A site is formed in part by the α phosphate of ATP, which has no analog in the PPi complex.

Ca^{2+} is a micromolar inhibitor of ATP synthesis, but is competitive with cAMP. However, since increase in Ca^{2+} from 2 to 5 μM is not accompanied by an appreciable decrease in AC activity, it is possible that Ca supports catalytic activity, possibly through interaction at the B site. The mechanism of this interaction requires further study.

Most vertebrate adenylyl cyclases, AC2, AC4 and AC7, for example, are not inhibited by micromolar Ca^{2+} . Molecular Modeling of the Type II AC CHD domain onto the open conformation of VC1:IIC2 structure (1AZS) reveals several non-conserved amino residues around the catalytic site. The insensitivity of Type II AC to sub-micromolar Ca^{2+} might be attributed to local features of the binding site (see supplemental figure S1 and S2). For example, substitution of Ala-409 of VC1 with Pro-307 of IIC1 might restrict the movement of $\alpha 1$ - $\alpha 2$ helices upon binding of Ca^{2+} to the B site.

In contrast to AC5, bicarbonate-activated soluble adenylyl cyclase (sAC) is stimulated by Ca^{2+} , which, with an $\text{EC}_{50} = \sim 750 \mu\text{M}$, decreases the K_M of the enzyme for ATP from 10 mM to 1 mM (57,58). Crystallographic studies of the homologous sAC from *Cyanobacteria* have revealed open and closed conformational states that approximate those observed in VC1:IIC2 (59). Structures of the *Cyanobacterial* sAC catalytic core in complex with ATP α S or AMP (CH) $_2$ PP and Ca^{2+} (or Ca^{2+} mimetics Sr^{+2} and Eu^{+3}) reveal exclusive binding of Ca^{2+} at the B metal site that leaves the Mg^{2+} site unoccupied. The *Cyanobacterial* sAC adopts an open conformation, particularly with respect to the $\beta 1$ - $\alpha 1$ element, that is similar to that of the Ca^{2+} -bound VC1:IIC2 complexes. However, ATP is tightly bound — with contacts to both nucleoside and phosphate moieties — in the open, Ca^{2+} -bound state of sAC. Thus, by stabilizing the nucleotide β — and γ — phosphates at the active site, the hepta-coordinate Ca^{2+} increases affinity for nucleotide, without fully destabilizing the metal A site for Mg^{2+} binding. We propose that global features of the catalytic site in the basal states of Class III ACs dictate their susceptibility to either activation or inhibition by Ca^{2+} . It is probable that these structural features, which determine the volume of the active site and disposition of purine, metal ion and phosphate binding residues, are determined by many residues at and surrounding the interface between the CHD domains.

The mechanisms by which AC activity is dynamically regulated by Ca^{2+} are complex, involving differential responses by various AC isoforms, contingent on patterns of tissue-specific expression. The data presented here, in the context of previous studies, reveal the molecular mechanism by which fluctuations in the physiological concentration of Ca^{2+} might directly attenuate cAMP production by AC5 and AC6.

Supplementary Material

Refer to Web version on PubMed Central for supplementary material.

ACKNOWLEDGMENT

We thank the staffs at the Advanced Proton Synchrotron SBC-CAT ID-19 beamline and the Stanford Synchrotron Radiation Laboratory for their assistance with data collection.

Abbreviations

AC, adenylyl cyclase
 mAC, mammalian membrane-bound adenylyl cyclase
 VC1 and IIC2, the N- and C-terminal catalytic domains from canine AC5 and rat type II AC respectively, expressed as soluble proteins
 G α s, stimulatory G-protein for AC
 FSK, forskolin
 MP-FSK, acetyl-7-[O-(N-methylpiperazino)- γ -butyryl]-forskolin
 sAC, soluble, bicarbonate-activated adenylyl cyclase
 EC_{50} , The molar concentration of Ca^{2+} , which produces 50% of the maximum AC activity.
 $[\text{Ca}^{2+}]$, calcium concentration
 ATP α S, adenosine 5'-[α (R $_p$)-thio]triphosphate

Ap(CH)pp, α,β -methyleneadenosine 5'-triphosphate
 GTP γ S, guanosine 5'-[γ -thio]triphosphate
 P_{Pi}, pyrophosphate
 2'-d-3'-AMP, deoxy, 3' adenosine monophosphate
 S.D., standard deviation.

REFERENCES

- (1). Sunahara RK, Dessauer CW, Gilman AG. Complexity and diversity of mammalian adenylyl cyclases. *Annu Rev Pharmacol Toxicol* 1996;36:461–480. [PubMed: 8725398]
- (2). Buck J, Sinclair ML, Schapal L, Cann MJ, Levin LR. Cytosolic adenylyl cyclase defines a unique signaling molecule in mammals. *Proc Natl Acad Sci U S A* 1999;96:79–84. [PubMed: 9874775]
- (3). Garbers DL, Johnson RA. Metal and metal-ATP interactions with brain and cardiac adenylate cyclases. *J Biol Chem* 1975;250:8449–8456. [PubMed: 1194261]
- (4). Zimmermann G, Zhou D, Taussig R. Mutations uncover a role for two magnesium ions in the catalytic mechanism of adenylyl cyclase. *J Biol Chem* 1998;273:19650–19655. [PubMed: 9677392]
- (5). Tesmer JGG, Sunahara RK, Johnson RA, Gilman AG, Sprang SR. Two metal ion catalysis in adenylyl cyclase. *Science* 1999;285:756–760. [PubMed: 10427002]
- (6). Krupinski J, Cali JJ. Molecular diversity of the adenylyl cyclases. *Adv Second Messenger Phosphoprotein Res* 1998;32:53–79. [PubMed: 9421585]
- (7). Hanoune J, Defer N. Regulation and role of adenylyl cyclase isoforms. *Annu Rev Pharmacol Toxicol* 2001;41:145–174. [PubMed: 11264454]
- (8). Cooper DM, Mons N, Karpen JW. Adenylyl cyclases and the interaction between calcium and cAMP signalling. *Nature* 1995;374:421–424. [PubMed: 7700350]
- (9). Guillou JL, Nakata H, Cooper DM. Inhibition by calcium of mammalian adenylyl cyclases. *J Biol Chem* 1999;274:35539–35545. [PubMed: 10585428]
- (10). Squire, LR.; Bloom, F.; McConnell, SK.; Roberts, JL.; Spitzer, N.; Zigmond, MJ. *Fundamental Neuroscience*. Vol. 2 ed.. Academic Press; San Diego: 2003.
- (11). Willoughby D, Cooper DM. Organization and Ca²⁺ regulation of adenylyl cyclases in cAMP microdomains. *Physiol Rev* 2007;87:965–1010. [PubMed: 17615394]
- (12). Cooper DM. Molecular and cellular requirements for the regulation of adenylate cyclases by calcium. *Biochem Soc Trans* 2003;31:912–915. [PubMed: 14505447]
- (13). Cooper DM, Karpen JW, Fagan KA, Mons NE. Ca(2+)-sensitive adenylyl cyclases. *Adv Second Messenger Phosphoprotein Res* 1998;32:23–51. [PubMed: 9421584]
- (14). Fagan KA, Mons N, Cooper DM. Dependence of the Ca²⁺-inhibitable adenylyl cyclase of C6-2B glioma cells on capacitative Ca²⁺ entry. *J Biol Chem* 1998;273:9297–9305. [PubMed: 9535924]
- (15). Tang W-J, Krupinski J, Gilman AG. Expression and characterization of calmodulin-activated (type I) adenylyl cyclase. *J Biol Chem* 1991;266:8595–8603. [PubMed: 2022671]
- (16). Xia Z, Storm DR. Calmodulin-regulated adenylyl cyclases and neuromodulation. *Curr. Opin. Neurobiol* 1997;7:391–396. [PubMed: 9232797]
- (17). Wu ZL, Thomas SA, Villacres EC, Xia Z, Simmons ML, Chavkin C, Palmiter RD, Storm DR. Altered behavior and long-term potentiation in type I adenylyl cyclase mutant mice. *Proc Natl Acad Sci U S A* 1995;92:220–224. [PubMed: 7816821]
- (18). Wayman GA, Impey S, Storm DR. Ca²⁺ inhibition of type III adenylyl cyclase in vivo. *J Biol Chem* 1995;270:21480–21486. [PubMed: 7665559]
- (19). Choi EJ, Xia Z, Storm DR. Stimulation of the type III olfactory adenylyl cyclase by calcium and calmodulin. *Biochemistry* 1992;31:6492–6498. [PubMed: 1633161]
- (20). Paterson JM, Smith SM, Simpson J, Grace OC, Sosunov AA, Bell JE, Antoni FA. Characterisation of human adenylyl cyclase IX reveals inhibition by Ca(2+)/Calcineurin and differential mRNA polyadenylation. *J Neurochem* 2000;75:1358–1367. [PubMed: 10987815]
- (21). Brostrom MA, Brotman LA, Brostrom CO. Calcium-dependent adenylate cyclase of pituitary tumor cells. *Biochim Biophys Acta* 1982;721:227–235. [PubMed: 6816295]

- (22). Caldwell KK, Boyajian CL, Cooper DM. The effects of Ca^{2+} and calmodulin on adenylyl cyclase activity in plasma membranes derived from neural and non-neural cells. *Cell Calcium* 1992;13:107–121. [PubMed: 1633609]
- (23). Colvin RA, Oibo JA, Allen RA. Calcium inhibition of cardiac adenylyl cyclase. Evidence for two distinct sites of inhibition. *Cell Calcium* 1991;12:19–27. [PubMed: 2015619]
- (24). Gu C, Cooper DM. Ca^{2+} , Sr^{2+} , and Ba^{2+} identify distinct regulatory sites on adenylyl cyclase (AC) types VI and VIII and consolidate the apposition of capacitative cation entry channels and Ca^{2+} -sensitive ACs. *J Biol Chem* 2000;275:6980–6986. [PubMed: 10702261]
- (25). Hu B, Nakata H, Gu C, De Beer T, Cooper DM. A critical interplay between Ca^{2+} inhibition and activation by Mg^{2+} of AC5 revealed by mutants and chimeric constructs. *J Biol Chem* 2002;277:33139–33147. [PubMed: 12065575]
- (26). Sinha SC, Sprang SR. Structures, mechanism, regulation and evolution of class III nucleotidyl cyclases. *Rev Physiol Biochem Pharmacol* 2007;160:105–140.
- (27). Tesmer JJG, Sunahara RK, Gilman AG, Sprang SR. Crystal structure of the catalytic domains of adenylyl cyclase in a complex with $\text{G}_{\text{so}} \bullet \text{GTP}\gamma\text{S}$. *Science* 1997;278:1907–1916. [PubMed: 9417641]
- (28). Dessauer CW, Gilman AG. The catalytic mechanism of mammalian adenylyl cyclase. Equilibrium binding and kinetic analysis of P-site inhibition. *J Biol Chem* 1997;272:27787–27795. [PubMed: 9346923]
- (29). Yoshimura M, Cooper DM. Cloning and expression of a Ca^{2+} -inhibitable adenylyl cyclase from NCB-20 cells. *Proc Natl Acad Sci U S A* 1992;89:6716–6720. [PubMed: 1379717]
- (30). Whisnant RE, Gilman AG, Dessauer CW. Interaction of the two cytosolic domains of mammalian adenylyl cyclase. *Proc Natl Acad Sci U S A* 1996;93:6621–6625. [PubMed: 8692867]
- (31). Sunahara RK, Dessauer CW, Whisnant RE, Kleuss C, Gilman AG. Interaction of G_{sa} with the cytosolic domains of mammalian adenylyl cyclase. *J Biol Chem* 1997;272:22265–22271. [PubMed: 9268375]
- (32). Tesmer, JJG.; Sunahara, RK.; Fancy, DA.; Gilman, AG.; Sprang, SR. *Methods in Enzymology*. 2002. Crystallization of complex between soluble domains of adenylyl cyclase and activated G_{sa} ; p. 198–206.
- (33). Mou TC, Gille A, Fancy DA, Seifert R, Sprang SR. Structural basis for the inhibition of mammalian membrane adenylyl cyclase by 2'-(3')-O-(N-Methylanthraniloyl)-guanosine 5'-triphosphate. *J Biol Chem* 2005;280:7253–7261. [PubMed: 15591060]
- (34). Linse S. Calcium binding to proteins studied via competition with chromophoric chelators. *Methods Mol Biol* 2002;173:15–24. [PubMed: 11859758]
- (35). Otwinowski Z, Minor W. Processing of x-ray diffraction data collected in oscillation mode. *Methods in Enzymology* 1997;276:307–326.
- (36). Brünger AT, Adams PD, Clore GM, Gros P, Grosse-Kunstleve RW, Jiang J-S, Kuszewski J, Nilges M, Pannu NS, Read RJ, Rice LM, Simonson T, Warren GL. Crystallography and NMR system (CNS): A new software suite for macromolecular structure determination. *Acta Cryst* 1998;D54:905–921.
- (37). Murshudov GN, Vagin AA, Dodson EJ. Refinement of macromolecular structures by the maximum-likelihood method. *Acta Crystallogr D Biol Crystallogr* 1997;53:240–255. [PubMed: 15299926]
- (38). Collaborative computational project, N. The CCP4 Suite: programs for protein crystallography. *Acta Crystallographica* 1994;D50:760–763.
- (39). Read RJ. Improved Fourier coefficients for maps using phases from partial structures with errors. *Acta Crystallographica* 1986;A42:140–149.
- (40). Jones TA, Zou JY, Cowan SW, Kjeldgaard M. Improved methods for the building of protein models in electron density maps and the location of errors in these models. *Acta Crystallogr* 1991;A47:110–119.
- (41). Emsley P, Cowtan K. Coot: model-building tools for molecular graphics. *Acta Crystallogr D Biol Crystallogr* 2004;60:2126–2132. [PubMed: 15572765]
- (42). Alvarez R, Daniels DV. A single column method for the assay of adenylate cyclase. *Anal Biochem* 1990;187:98–103. [PubMed: 2164795]

- (43). Alvarez R, Daniels DV. A separation method for the assay of adenylylcyclase, intracellular cyclic AMP, and cyclic-AMP phosphodiesterase using tritium-labeled substrates. *Anal Biochem* 1992;203:76–82. [PubMed: 1326236]
- (44). Boyajian CL, Garritsen A, Cooper DM. Bradykinin stimulates Ca^{2+} mobilization in NCB-20 cells leading to direct inhibition of adenylylcyclase. A novel mechanism for inhibition of cAMP production. *J Biol Chem* 1991;266:4995–5003. [PubMed: 1848232]
- (45). Ahljianian MK, Cooper DM. Antagonism of calmodulin-stimulated adenylate cyclase by trifluoperazine, calmidazolium and W-7 in rat cerebellar membranes. *J Pharmacol Exp Ther* 1987;241:407–414. [PubMed: 3106618]
- (46). Salomon Y, Londos C, Rodbell M. A highly sensitive adenylate cyclase assay. *Anal Biochem* 1974;58:541–548. [PubMed: 4827395]
- (47). Segel, I. *Enzyme Kinetics; Behavior and Analysis of Rapid Equilibrium and Steady-State Enzyme Systems*. John Wiley & Sons; New York: 1975.
- (48). Sunahara RK, Beuve A, Tesmer JJG, Sprang SR, Garbers DL, Gilman AG. Exchange of substrate and inhibitor specificities between adenylyl and guanylyl cyclases. *J. Biol. Chem* 1998;273:16332–16338. [PubMed: 9632695]
- (49). Tucker CL, Hurley JH, Miller TR, Hurley JB. Two amino acid substitutions convert a guanylyl cyclase, RetGC-1, into an adenylyl cyclase. *Proc Natl Acad Sci U S A* 1998;95:5993–5997. [PubMed: 9600905]
- (50). Strynadka NCJ, James MNG. Crystal structures of the helix-loop-helix calcium-binding proteins. *Annual Review of Biochemistry* 1989;58:951–998.
- (51). Tang WJ, Stanzel M, Gilman AG. Truncation and alanine-scanning mutants of type I adenylyl cyclase. *Biochemistry* 1995;34:14563–14572. [PubMed: 7578062]
- (52). Yan S-Z, Huang Z-H, Shaw RS, Tang W-J. The conserved asparagine and arginine are essential for catalysis of mammalian adenylyl cyclase. *J Biol Chem* 1997;272:12342–12349. [PubMed: 9139678]
- (53). Tesmer JJ, Dessauer CW, Sunahara RK, Murray LD, Johnson RA, Gilman AG, Sprang SR. Molecular basis for P-site inhibition of adenylyl cyclase. *Biochemistry* 2000;39:14464–14471. [PubMed: 11087399]
- (54). Mou TC, Gille A, Suryanarayana S, Richter M, Seifert R, Sprang SR. Broad specificity of mammalian adenylyl cyclase for interaction with 2',3'-substituted purine- and pyrimidine nucleotide inhibitors. *Mol Pharmacol* 2006;70:878–886. [PubMed: 16766715]
- (55). Steitz TA. DNA- and RNA-dependent DNA polymerases. *Curr. Opin. Struct. Biol* 1993;3:31–38.
- (56). Sutton RB, Sprang SR. Crystal structure of the calcium-dependent phospholipid binding domain from protein kinase C- β in a ternary Ca^{2+} complex. *Structure*. 1998
- (57). Jaiswal BS, Conti M. Calcium regulation of the soluble adenylyl cyclase expressed in mammalian spermatozoa. *Proc Natl Acad Sci U S A* 2003;100:10676–10681. [PubMed: 12958208]
- (58). Litvin TN, Kamenetsky M, Zarifyan A, Buck J, Levin LR. Kinetic properties of “soluble” adenylyl cyclase. Synergism between calcium and bicarbonate. *J Biol Chem* 2003;278:15922–15926. [PubMed: 12609998]
- (59). Steegborn C, Litvin TN, Levin LR, Buck J, Wu H. Bicarbonate activation of adenylyl cyclase via promotion of catalytic active site closure and metal recruitment. *Nat Struct Mol Biol* 2005;12:32–37. [PubMed: 15619637]

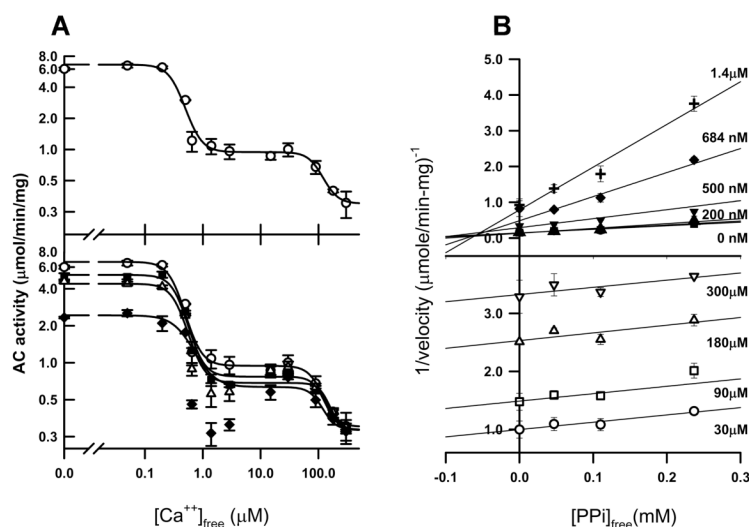


Figure 1.

Biphasic inhibition of VC1:IIC2 activity in the presence and absence of pyrophosphate. (A) Activity of VC1 (50 nM), IIC2 (250 nM) in the presence of 500 nM $G_{\alpha s}$ •GTP γ S, and 10 μ M FSK was determined in the absence (\circ ; upper panel) or presence (lower panel) of a concentration of PPI sufficient to inhibit AC activity by 25%, 50% or 75% (47 μ M; (\blacksquare), 115 μ M; (\triangle), or 235 μ M; (\blacklozenge), respectively). Data represent the mean \pm S.D. of at least 3 independent experiments, and were fit to a two-site competition model. (B) Dixon plot to show the relation between the sub-micromolar (upper panel) or surpa-micromolar concentration (lower panel) of Ca^{2+} and PPI. The data were recast from the Ca^{2+} inhibition of AC activity that were determined in the absence or presence of a concentration of PPI. \bullet , no added calcium; \blacktriangle , $[Ca^{2+}]_{free}=200$ nM; \blacktriangledown , $[Ca^{2+}]_{free}=500$ nM; \blacklozenge , $[Ca^{2+}]_{free}=684$ nM; $+$, $[Ca^{2+}]_{free}=1.40$ μ M; \circ , $[Ca^{2+}]_{free}=30$ μ M; \square , $[Ca^{2+}]_{free}=90$ μ M; \triangle , $[Ca^{2+}]_{free}=180$ μ M; ∇ , $[Ca^{2+}]_{free}=300$ μ M. For some data points, the width of the error bars is smaller than the symbol.

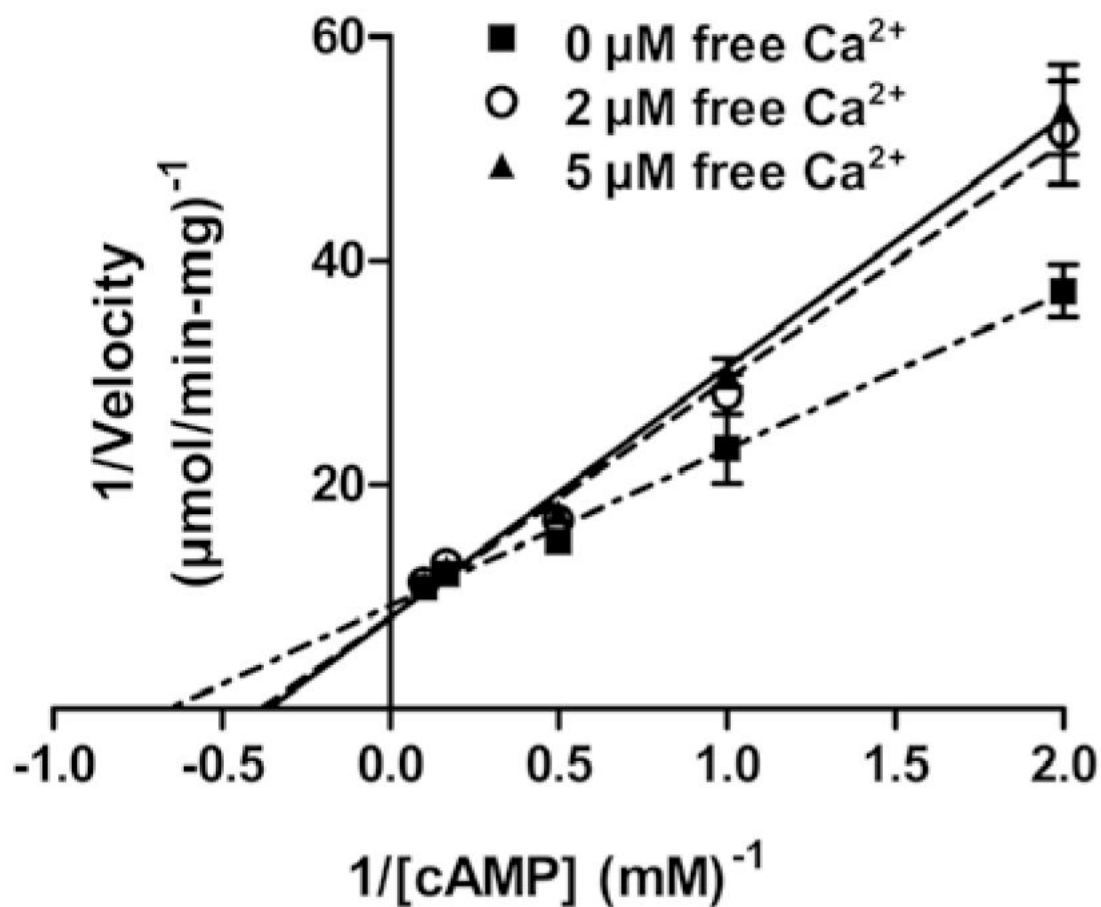


Figure 2. Ca^{2+} inhibition of ATP synthesis. Double reciprocal plots for inhibition by Ca^{2+} of ATP synthesis by VC1 (0.4 μM), IIC2 (2 μM) and 1 μM $\text{G}\alpha\text{s}\cdot\text{GTP}\gamma\text{S}$; Reactions were conducted in the absence (\blacksquare) of Ca^{2+} or in the presence of 2 μM (\circ), or 5 μM (\blacktriangle) free Ca^{2+} .

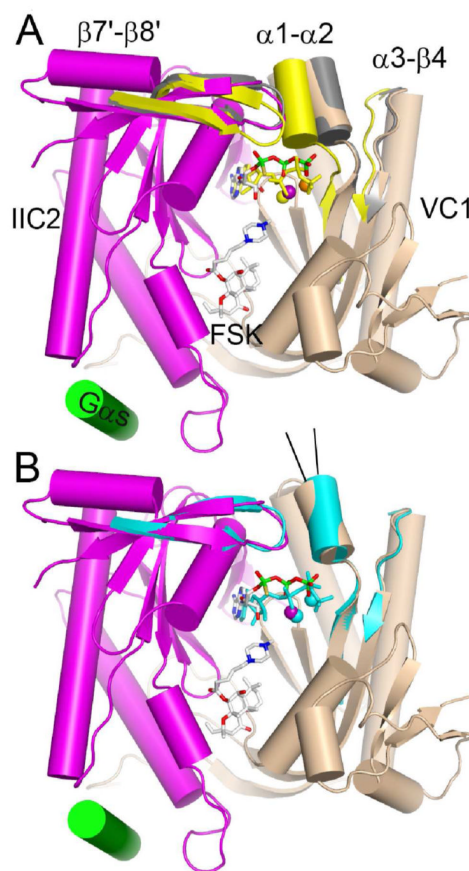


Figure 3.

Global views of $G\alpha_s$ •GTP γ S/FSK-activated VC1:IIC2 substrate complexes with Ca^{2+} or Mg^{2+} . (A) The structure of VC1 and IIC2 domains in the ATP γ S• Ca^{2+} complex shown in *mauve* and *tan*, respectively (26). Shown in superposition are the secondary structure elements $\beta 1$ — $\alpha 1$ — $\alpha 2$ and $\alpha 3$ — $\beta 4$ of VC1 and $\beta 7'$ — $\beta 8'$ of IIC2 in the open-state VC1:IIC2 apoenzyme (PDB code:1AZS), *gray*, and those of the closed-state ATP α S complex with Mn^{2+} and Mg^{2+} (PDB code:1CJK), *yellow* (26,27). The switch II helix of GTP γ S-activated $G\alpha_s$ subunit is shown as a red cylinder. Ligands are drawn as stick models; for ATP α S and FSK, carbon atoms are *gray*, nitrogens *blue*, oxygens *red*, and phosphorus *green*. Metal ions are shown as metallic spheres; Ca^{2+} ion is *violet*, Mg^{2+} *light-yellow*, and Mn^{2+} *orange*. This coloring scheme for atoms is retained in all figures unless otherwise noted. (B) Superposition of the secondary structure elements $\beta 1$ — $\alpha 1$ — $\alpha 2$ and $\alpha 3$ — $\beta 4$ of VC1 and $\beta 7'$ — $\beta 8'$ of IIC2 of the ATP•2Ca complex with two Ca^{2+} ions *cyan* with the VC1 and IIC2 domains structure of ATP α S•Ca, using atomic coloring scheme as in panel A. The two structures are similar to each other except that the $\alpha 1$ helix of ATP α S•Ca complex is rotated $\sim 10^\circ$ toward the IIC2 domain relative to the $\alpha 1$ helix of ATP•2Ca complex [as shown by the lines indicating $\alpha 1$ helix axis in two structures].

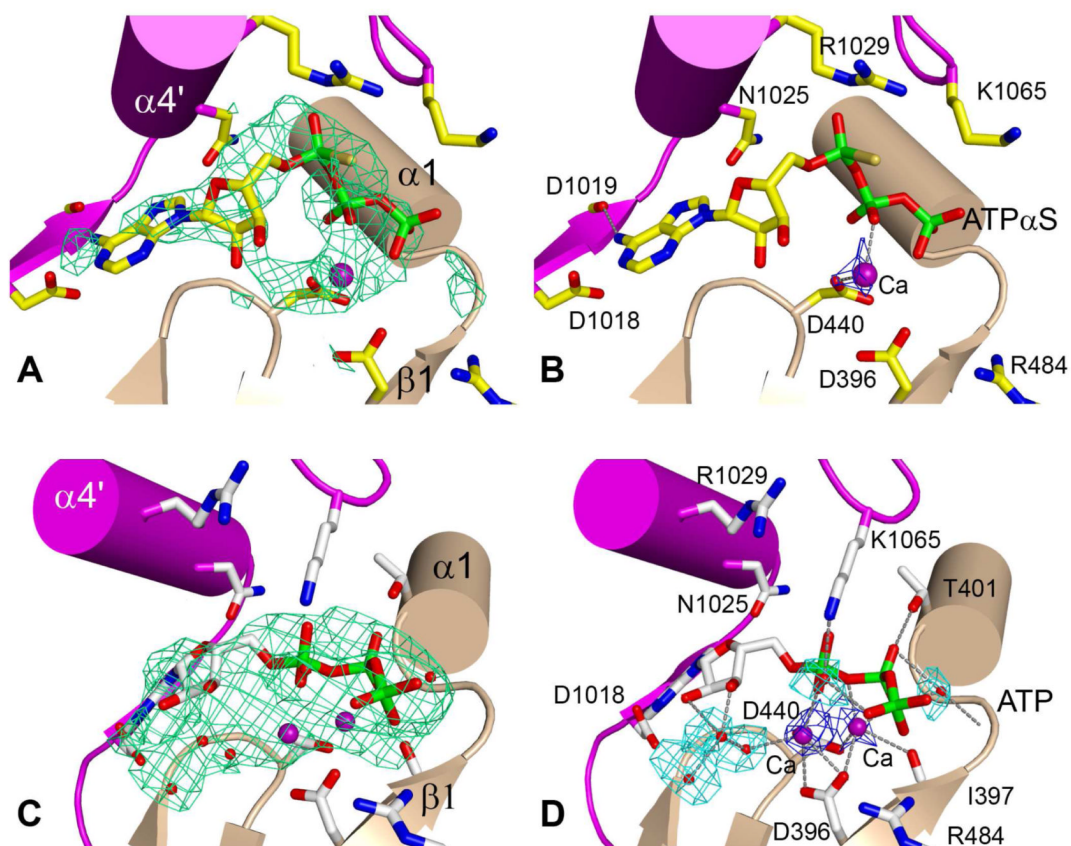


Figure 4.

Binding of ATP and the inhibitor ATP α S to AC in the presence of high (1.5 mM) or low (8 μ M) Ca $^{2+}$. Gas•GTP γ S/FSK-activated VC1:IIC2 bound to (A) ATP α S and Ca $^{2+}$, or (C) ATP and two Ca $^{2+}$ ions. The nucleotide, Ca $^{2+}$ ions, and water molecules are shown as stick models or spheres. The 3.0 Å or 2.9 Å $|F_o| - |F_c|$ electron density maps, computed from the refined model from which coordinates for the Ca $^{2+}$ and nucleotide in the ATP α S•Ca or ATP•2Ca complexes, respectively, are omitted and contoured at the 2.5 σ level, is shown as *lime-green* wire cages. Side chains of protein residues in the catalytic site are shown as sticks. The network of non-bonded interactions among (B) ATP α S and Ca $^{2+}$, or (D) ATP, the two Ca $^{2+}$ ions, water molecules, and side chains of protein residues are shown. Individual calcium ion(s) and water molecules are positioned according to the $|F_o| - |F_c|$ difference electron density maps calculated with the respective atoms omitted from the phasing model or Ca replaced with water. The difference maps for Ca $^{2+}$ ion(s) and waters are contoured at the 3.0 σ and 2.5 σ level and shown as *blue* and *cyan* wire cages, respectively. The *gray* dashed lines depict hydrogen bonds (<3.2 Å) and metal coordination contacts (<3.0 Å) between ligand atoms, metal ions, water molecules, and protein residues. The hydrogen bonds, metal coordination contacts, single letter amino acid code, and residue ID numbers are shown for active site residues in this figure and in Figure 5 and 6.

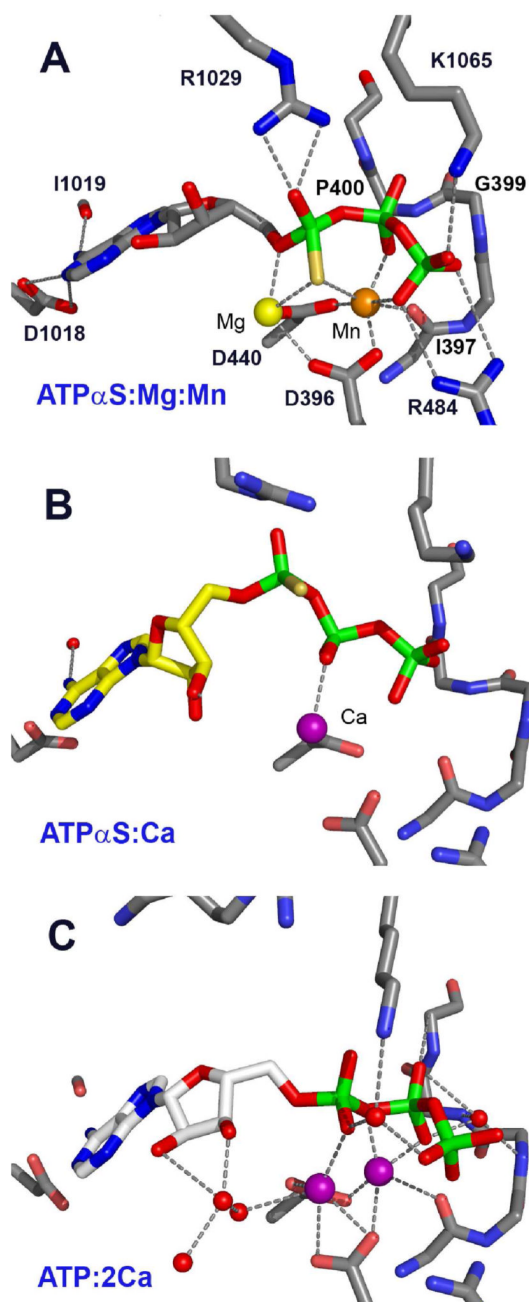


Figure 5.

ATP or ATP α S coordination with Mg $^{2+}$ or Ca $^{2+}$ in the catalytic site of VC1:IIC2. (A) ATP α S:Mg $^{2+}$ /Mn $^{2+}$ (PDB ID 1CJK); (B) ATP α S•Ca; (C) ATP•2Ca. The main chain of the phosphate-binding loop (Ile-397—Thr-401 of VC1) and the side chains of substrate and metal ion interacting residues are shown, and colored according to the scheme in Figure 4, except that carbon atoms are gray, yellow, and white for ATP α S with Mg $^{2+}$, ATP α S with Ca $^{2+}$, and ATP, respectively.

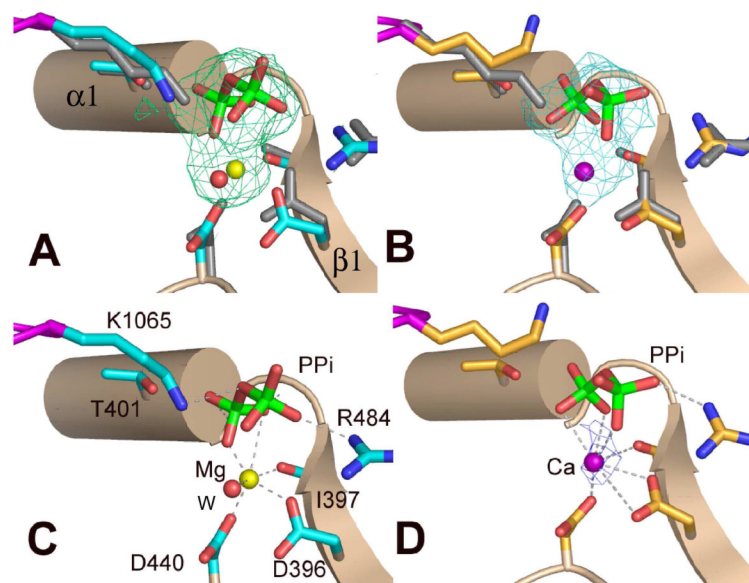


Figure 6.

VC1:IIC2 complexes with $\text{PPi} \cdot \text{Ca}^{2+}$ and $\text{PPi} \cdot \text{Mg}^{2+}$. Electron density $|F_o| - |F_c|$ omit maps are shown as *lime-green* wire cages that were calculated at the respective final resolution and contoured at the 2.5σ level for (A) the $\text{PPi} \cdot \text{Mg}^{2+}$ and (B) the $\text{PPi} \cdot \text{Ca}^{2+}$ complex. Models of PPi with Mg^{2+} or Ca^{2+} at the B site are shown as stick models and spheres. A water molecule is observed adjacent to the Mg^{2+} at the B site, but no significant electron density is observed at the metal A site in either structures. Stick models of side chains of protein residues from the open conformation (1AZS) of VC1:IIC2 were superimposed onto both structures and depicted as *gray*-colored side chains. Interactions of $\text{PPi} \cdot \text{Mg}^{2+}$ and $\text{PPi} \cdot \text{Ca}^{2+}$ with the AC catalytic site residues are shown in panels (C) and (D), respectively. The 2.8 \AA or 2.7 \AA $|F_o| - |F_c|$ electron density maps for the $\text{PPi} \cdot \text{Mg}^{2+}$ or $\text{PPi} \cdot \text{Ca}^{2+}$ complexes, respectively, are contoured at the 2.5σ level and shown as *lime-green* wire cages. In panel D, the *blue* wire cage represents electron density contoured at 3.0σ for the 2.8 \AA $|F_{oCa}| - |F_{oMg}|$ omit map, indicating that Ca^{2+} binds at site B. The VC1:IIC2 product complex with pyrophosphate and Mg^{2+} is, like that with Ca^{2+} , in the open conformation. Ligand and side chain atoms of protein residues are drawn as stick models with carbon atoms colored in *cyan* or *orange* for the $\text{PPi} \cdot \text{Mg}^{2+}$ or $\text{PPi} \cdot \text{Ca}^{2+}$ complexes, respectively.

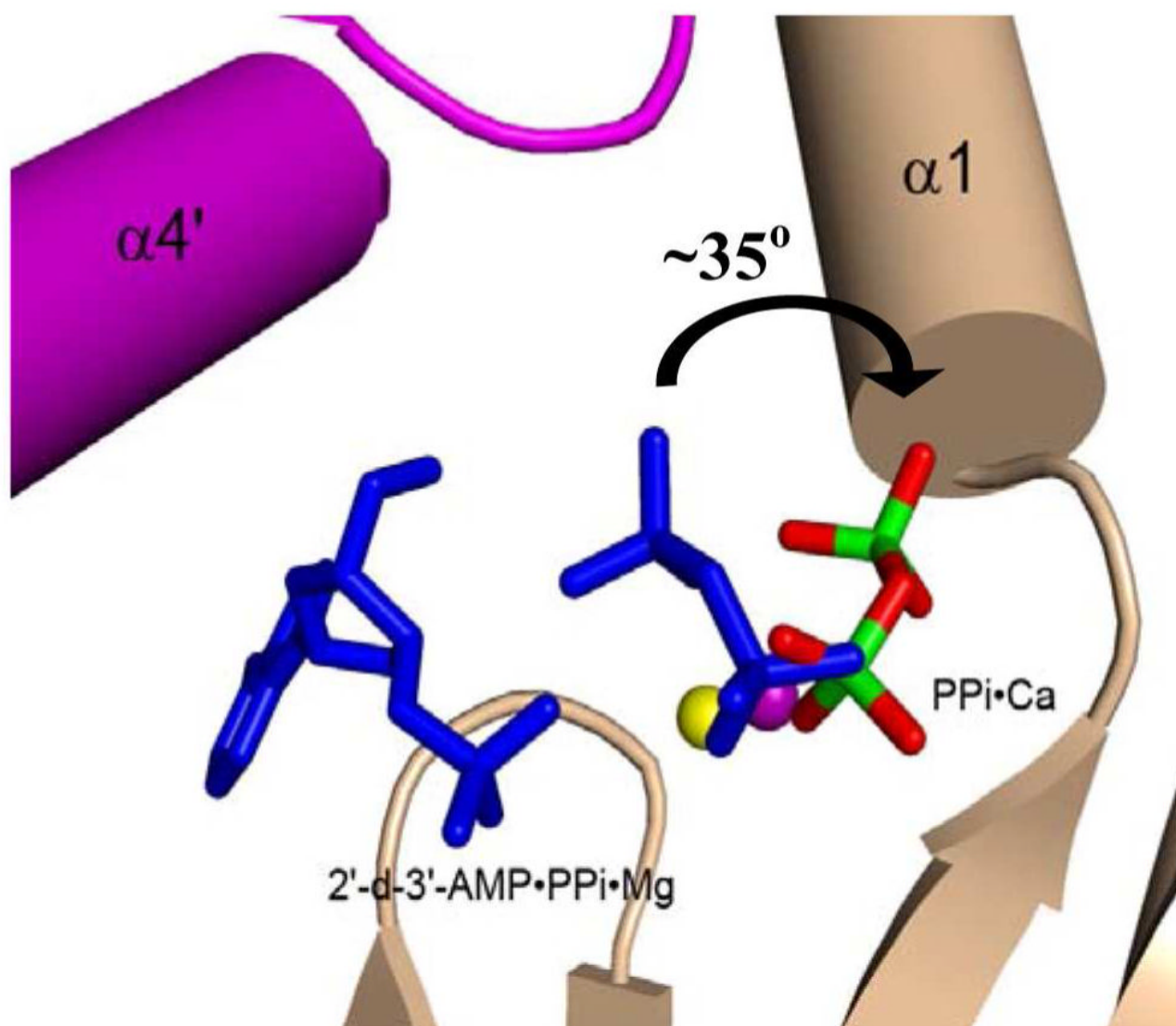


Figure 7.

A detailed view of 2'-d-3'-AMP•PPi•Mg²⁺ and PPi•Ca²⁺ complexes in the catalytic site of the superimposed complexes. The PPi is rotated ~35° toward to the β1-α1 loop of VC1 relative to the pyrophosphate moiety of 2'-d-3'-AMP•PPi•Mg²⁺ complex (PDB code:1CS4). Calcium ion in the complex with PPi occupy the B site as does Mg²⁺ in the complex with 2'-d-3'-AMP•PPi (shown in *blue*).

Table 1

Summary of data collection and refinement statistics

parameters	AC•ATP•2Ca ²⁺	AC•ATP•S•Ca ²⁺	AC•PPi•Ca ²⁺	AC•PPi•Mg ²⁺
cell constants (Å)				
<i>a</i>	118.3	118.7	117.9	117.5
<i>b</i>	133.5	133.7	133.0	133.1
<i>c</i>	70.7	71.0	70.0	70.1
<i>d</i> _{min} (Å)	2.9	3.0	2.7	2.8
Avg. redundancy	2.5 (2.1)	2.8 (2.1)	5.2 (3.0) ^d	3.1 (2.4)
<i>R</i> _{sym} (%)	17.6 (55.2)	17.5 (41.4)	12.5 (33.4)	13.9 (43.5)
completeness (%)	91.7 (87.6)	82.7 (67.5)	95.9 (89.7)	91.7 (86.4)
<I>/<σ>	6.5 (1.2)	5.1 (1.6)	9.9 (2.2)	7.2 (1.8)
resolution range for refinement ^c (Å)	15-2.9	15-3.0	15-2.7	15-2.8
total reflections used	21380	18290	28220	23685
no. protein atoms	5637	5627	5638	5691
no. water molecules	6	12	33	12
no. heterogen atoms	94	106	73	73
rmsd bond length (Å)	0.008	0.012	0.007	0.008
rmsd bond angle (°)	1.100	1.453	1.102	1.128
<i>R</i> _{work} ^d (%)	24.9	23.9	24.5	23.7
<i>R</i> _{free} ^e (%)	29.9	30.9	29.1	29.2
Avg overall B—factor (Å ²)	40.6	31.84	51.2	54.1
Avg B—factor on substrate (Å ²)	52.1	85.0	67.8	71.4
Avg B—factor on metal ion(s) (Å ²)	43.9	66.7	63.6	67.5
Ramachandran plot (%)				
Favorable and allowed region	100	99.7	99.5	99.8
Generously allowed region	0	0.3	0.5	0.2

^aNumbers in parentheses refer to data in the highest resolution shell.^b $R_{\text{Sym}} = \sum_h \sum_i |I(h) - \langle I(h) \rangle| / \sum_h \sum_i I(h)_i$ where $I(h)$ is the mean intensity after rejections.^cDue to anisotropy, data with l index greater than 20 were omitted from refinement.^d $R_{\text{work}} = \sum_h \|F_o(h) - |F_c(h)|\| / \sum_h |F_o(h)|$, where $F_o(h)$ and $F_c(h)$ are observed and computed structure factors; no l -o cutoff was used during refinement.

^e 5% of the complete data set was excluded from refinement to calculate R_{free} .